Model instability and channel connectivity for 2D coastal marsh simulations

Z. Li[1], B. R. Hodges[1]

Z. Li: zhili@utexas.edu; B. R. Hodges hodges@mail.utexas.edu

[1] Center for Water and the Environment, University of Texas at Austin, Austin, TX, USA

Abstract

Reduced freshwater inflow into a coastal marsh can result in environmental stress through episodic hypersalinity. Hydrodynamic models can be used to evaluate salinity-control strategies when freshwater supplies are constrained by climate or increasing urban demands. However, there remain significant scientific, engineering, and technical barriers to correctly modeling salinity transport in such systems. In particular, the numerical instability at the wetting/drying front caused by strong wind stress and steep surface gradient and the inappropriate representation of the complex channels at practical computational scales are unsolved problems. This study documents recent achievements in modeling the time–space evolution of shallow marsh salinity using the Fine Resolution Environmental Hydrodynamic model (Frehd) applied to the Nueces River Delta (Texas, USA). The 2D depth-integrated model is tested across a variety of bathymetric representations derived from high-resolution lidar data to evaluate the effects of grid refinement and a variety of bathymetry processing methods. Novel treatments are proposed and tested to suppress unrealistic velocities and scalar concentrations caused by rapid wetting/drying and strong wind stress. The model results are compared with the field data collected at 12 spatially-distributed locations across the marsh, yielding good model-data agreements for free surface elevation and reasonable agreements for salinity. Analyses of results indicate that the critical difficulty for capturing salinity transport is in correctly representing connectivity effects (both blocking and channel features) at fine scales on the coarse grid without overestimating fluxes. Modeled water surface elevations are relatively robust to poor representation of connectivity whereas the salinity distribution is strongly affected, particularly at key choke points. This study defines a set of future challenges in developing automated methods for evaluating and preserving geometric connectivity at practical model grid resolution.

Keywords

Shallow coastal marsh, Numerical modeling, Bathymetric error, Salinity transport

1 Introduction

Hydrologic modification of river flows and sea level rise are combined threats to the viability of many freshwater/saltwater marsh ecosystems (e.g. [18, 41, 51]). Both effects push upstream the salt/fresh mixing zones, often into narrower, confined areas with inhospitable geomorphology of steeper

gradients and incised channels. Marsh systems are critical for many estuarine and coastal species that have limited salinity tolerance as juveniles, so the upstream migration and reduction in brackish marsh areas will potentially reduce nursery habit and impact the ecosystem balance both offshore and within the estuary itself. Understanding and quantifying the salinity exchange in these systems with field data alone is difficult due to the myriad of flow pathways, which necessarily requires numerous sensors distributed widely over the marsh that are emplaced for months to years. Numerical models thus become popular tools aiding in marsh salinity research.

The present work is motivated by difficulties encountered in modeling salinity transport in a shallow marsh, the Nueces River Delta (Texas, USA). This shallow marshland (with depth on the order of 1 m) is located northwest of Nueces Bay, an extension of Corpus Christi Bay along the Texas coast (Fig. 1). The main channel through the marshes and down to Nueces Bay is known as the Rincon Bayou, which was separated from the Nueces River main stem. Because Nueces Bay is micro-tidal (typical daily range of 0.3 m), the tidal flux into the delta is insufficient to turn the marshland into a simple well-flushed saltwater system. Instead, the combination of limited freshwater inflows, poor tidal flushing, and high evaporation rates results in inverse estuary effects that have caused episodic hypersalinity in the upper marsh [1]. Infrastructure efforts to improve freshwater flushing (see Fig. 1) have included physically modifying connectivity of the system with the Nueces Overflow Channel (NOC), the Rincon Bayou Overflow Channel (ROC) and directly pumping freshwater into the delta through the Rincon Bayou Pipeline [19]. The pumping system is an unusual step in marsh restoration, and is capable of delivering 3.7×10^{6} m^{3} d^{-1} (3000 ac-ft per day) of freshwater from just upstream of the Calallen dam (Fig. 1) on the Nueces main stem to the upper end of the Rincon Bayou. Field studies show that the pumping system is effective in flushing hypersalinity through the main channels of the Rincon Bayou [19, 36]. However, there remain open questions as to the best flow rates, pumping durations, and event timing to optimize the effect of the fresh water available that have to be answered with the assistance of numerical modeling.

Numerical models for coastal marshes require three increasingly challenging levels of reliability: (i) the model must be numerically stable, (ii) the surface flux connectivity should be reasonably represented, and (iii) the net salinity transport should provide residence time and salinity distributions that are statistically similar to observations. In deep estuaries with limited wetting/drying, model stability and path connectivity requirements are often easily satisfied, so research has focused on the third requirement (e.g., studies on residence time [40], tidal intrusion [34], turbulence closures and high-order schemes [14]). However, for shallow coastal marshes with frequent wetting/drying the first two requirements are challenging in themselves. In terms of model stability, it is well-recognized that modeling

the wetting/drying of marshland can affect the maximum size of the stable time step and hence the practicality of a model [27, 31]. We have also identified (as discussed herein) a range of other issues that affect model stability including the interaction of small depths (which cannot be neglected in a marsh) and wind-driven fluxes that send conventional modeling algorithms unstable or produce unrealistic velocities unless extraordinarily small time steps are taken. As to connectivity, it has been demonstrated that it is a non-trivial task to produce a bathymetry at a practical modeling resolution (e.g., 15×15) that maintains the continuity of blocking features (e.g., levees) that are evident at 1×1 m lidar data [22]. This idea is extended to the challenges of representing channels, or in general any small but hydraulically important topographical feature that might not be fully captured by the model grid. Failure to correctly capture the channels and blockages can interrupt surface connectivity and to completely different hydrodynamic behaviors [10, 45, 48].

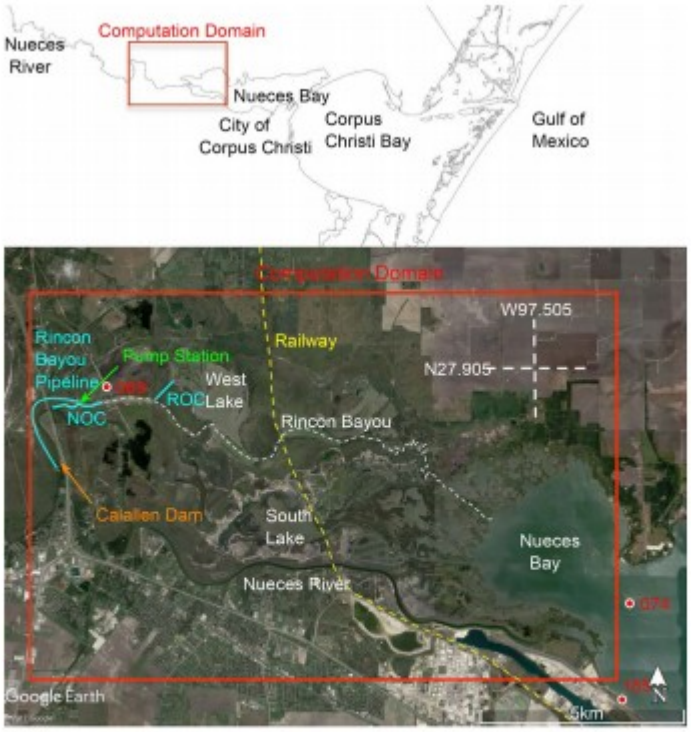

Fig. 1 Nueces delta study site with locations of the Rincon Overflow Channel (ROC), Nueces Overflow Channel (NOC) and Rincon Bay Bayou Pipeline. Sites 069, 074, 185 are long-term monitoring stations. Note that West Lake and South Lake are actually periodically-inundated tidal flats rather than lakes. Texas coastline from ArcGIS online, satellite image from Google Earth

With reference to the three requirements of coastal marsh models discussed above, the focus of the present work is in developing practical approaches for handling the model stability and system connectivity problems with salinity transport used as a means of evaluating the effectiveness of the methods. We use a high-resolution hydrodynamic model for the Nueces Delta to demonstrate the efficacy of our new methods and evaluate how

spatial resolution affects the model results. This system was selected because of its importance in a real-world water management problem and the availability of a data set with 15 months of salinity and depth measurements at broadly-distributed locations [39].

The modeling methods used herein are presented in Sect. 2, including a brief introduction of the Frehd hydrodynamic and transport model (Sect. 2.2). The approach to wetting/drying is found in Sect. 2.4; a novel method for wind-driven thin-layer flows is found in Sect. 2.5 and approaches to handle bathymetric connectivity at various scales are presented in Sect. 2.8. These specific issues are often given little attention in the numerical literature when a model is presented, but are critical to the performance in modeling marsh systems. The model setup for the Nueces Delta test case is illustrated in Sect. 3, which includes descriptions of the field-data collection (Sect. 3.1) as well as the tested model scenarios with different conditions for stability treatment (Sect. 3.2), spatial resolution and channel delineation (Sect. 3.3). The simulation results are analyzed in Sect. 4 by comparing to extensive field observations across the delta. The major findings are summarized in the conclusion, Sect. 5. Minor aspects such as the model spin-up and calibration are presented in the “Appendix”.

2 Numerical methods

2.1 Overview

This study uses a numerical model that is driven by and compared to a suite of observations of the delta and surroundings. The model is an updated version of the Nueces Delta Hydrodynamic Model (NDHM) [38]. The NDHM is a 2D version of the 3D Fine Resolution Environmental Hydrodynamic Model, which we call “Frehd” for readability. This model is a descendent of TRIM [7] and ELCOM [23] semi-implicit models with optional adaptions for 2nd-order accuracy [24, 25, 37], non-hydrostatic effects [49] and edge-blocking in complex topography [22]. A brief description of the model foundations is provided in Sect. 2.2.

In general, the semi-implicit numerical method is unconditionally linearly stable for any barotropic (wave speed) Courant–Friedrich–Lewy (CFL_B) number, and is conditionally stable in the advective CFL_A [7]. Practical experience has shown that momentum stability is retained for $CFL_A > 1$ in limited space-time locations as long as the the majority of the domain is at $\mathrm{CFL}_A < \sqrt{2}/2$ and care is taken with the nonlinear terms. The discrete scalar advection, Eq. (3), is an explicit finite-volume advance that strictly requires $CFL_A<1$ everywhere for both mass conservation and stability. In general, the semi-implicit approach for momentum is robust to an occasional high-CFL_A transient as the implicit free surface solution serves to damp and re-distribute effects of localized instabilities. Similarly, smaller perturbations of scalar concentrations caused by localized hydrodynamic instabilities can be neglected if they do not grow and scalar distributions remain within

physical ranges. Unfortunately, the combination of thin layers, wind-driven flows, and wetting/drying across a marsh can lead to high velocities (both real and unreal) in a simulation that can develop into catastrophic instability. In our experience, trying to reduce the global time step to maintain stability in a high-resolution marsh simulation results in absurdly small time steps that are simply impractical for the seasonal-to-annual time frames that are of interest. We have investigated approaches to using local subtime-stepping in lakes [20] and broader estuaries [17] , but to date have not been able to efficiently implement these approaches in the coastal marsh simulations. In the present work we focus on measures to identify and address the causes of instabilities rather than refining the time step to resolve the flow. Our philosophical argument for this approach is that resolving the flow associated with instabilities in a marsh is of little importance given their localized time/space locations—especially in consideration of the uncertainty and approximations of the system geometry at practical model grid scales. Thus, we seek methods to prevent instabilities by constraining the solution with physically plausible bounds. We have identified three key sources of instability and developed measure to address each: (i) instability caused by flow reversal, Sect. 2.3, (ii) instability due to wetting/drying Sect. 2.4, and (iii) instability due to wind-driven thin layers Sect. 2.5. These measures are necessary, but not entirely sufficient to ensure stable solutions, so we have added an *ad hoc* approach to truncating nonlinear terms (Sect. 2.6) to prevent a locally-high CFL from being propagated forward in time.

Simulating system connectivity in a channelized marsh is an interesting challenge as we often have finer-resolution digital elevation models (e.g., lidar) than we can practically represent in a simulation. The relative coarseness of the mesh has implications for the advective discretization, which can be readily solved as discussed in Sect. 2.7. More difficult is ensuring that a (relatively) coarse model mesh has a reasonable representation of the channel connectivity, flow areas, and blockages—i.e., a question of upscaling to maintain hydrodynamics and transport. In Sect. 2.8 we apply a concept of positive and negative objects that can be identified and modeled with automated processes. This approach provides some success, as discussed in Sect. 4, but there remains a number of outstanding issues (see Sect. 5).

2.2 Model foundations

The NDHM is a semi-implicit, volume-conservative implementation of the depth-integrated, hydrostatic Navier–Stokes (shallow water) equations on a rectilinear (structured) Cartesian grid. Momentum is:

$$\frac{\partial u_j}{\partial t} + u_k \frac{\partial u_j}{\partial x_k} = -g \frac{\partial \eta}{\partial x_j} + \frac{\partial}{\partial x_k}\left(\nu \frac{\partial u_j}{\partial x_k}\right) + \frac{\tau_{wj} - \tau_{bj}}{\rho h}, \quad : \quad j,k \in \{1,2\} \qquad (1)$$

where η is the free surface elevation, u_j are depth-averaged velocities, x_j are the corresponding Cartesian axes, h is the depth, ρ is the local density, ν is an eddy viscosity, and τ_{wj},τ_{bj} are the wind and bottom stress boundary conditions in the x_j direction. Note that the discretization of the boundary stresses has effects on model stability, as discussed in Sect. 2.3, below.

For Eq. 1, the depth at a grid cell center is defined as $h=\eta-b$, where b is the local bottom elevation above a baseline (herein NAVD88). Although Frehd includes governing equations for 3D flow and baroclinic forcing, herein the depth-integrated effect of salinity on density is neglected as it does not significantly contribute to advective fluxes in a shallow marsh. The momentum equations are closed by the depth-integration of the kinematic boundary condition applied to continuity [8], resulting in

$$\frac{\partial \eta}{\partial t} + \frac{\partial h u_k}{\partial x_k} = 0 \qquad (2)$$

Salinity transport is modeled with a standard advection-diffusion equation for incompressible flow:

$$\frac{\partial C}{\partial t} + u_k \frac{\partial C}{\partial x_k} = \frac{\partial}{\partial x_k}\left(\kappa \frac{\partial C}{\partial x_k}\right) \qquad (3)$$

where C is the salt concentration (kg/m^3) and κ is the turbulent diffusivity. Although the baseline Frehd model includes a variety of turbulence closures, for simplicity the NDHM uses a uniform, constant, small value of $\nu=10^{-4}$m^2/s. This simplification is reasonable where numerical diffusion associated with low-order advection scheme (see Sect. 2.7) provides significant horizontal mixing [15, 48]. Furthermore, for shallow estuaries, fluxes could be controlled by bottom stress and topographical restrictions rather than horizontal shear in the velocity field. In keeping with this simple approach, for the salinity we use $\kappa=\nu$, which is equivalent to setting the turbulent Schmidt number to unity.

Frehd follows the approach of [6] in using uniform Cartesian grid cells with an Arakawa-C stencil where the governing equations are solved for velocities on cell faces whereas surface elevations and scalar concentrations are solved on cell centers. The bathymetry is represented as a standard “z-level” system where the bottom elevation at the cell center is considered a uniform value across the entire cell. A finite-volume formulation is used in continuity (Eq. 2) and scalar transport (Eq. 3) so that volume and scalar mass are conserved to numerical precision (the latter as long as $CFL_A<1$). The advection terms are finite-difference discretizations, so the overall method is a hybrid finite difference/volume approach. The details of the Frehd discretization are similar to the semi-implicit approach described in [6] and [7], except where otherwise noted herein.

Frehd includes several choices for nonlinear terms in advection, Eq. (1), and scalar transport, Eq. (3). The choice of discretization is inherently tied to the

bathymetric resolution, and is discussed in Sect. 2.7, below. The diffusion terms for momentum and scalar diffusivity are discretized with central difference stencils.

For time-marching, Frehd offers the choice of the standard semi-implicit "theta method" [7] that is almost (but not quite) 2nd-order accurate [24], or a predictor-corrector method that is fully 2nd-order [25]. In keeping with 1st-order upwind scheme (see Sect. 2.7), herein we use a simple 1st-order θ=1 method, which is a 3-step method consisting of (1) a non-conservative, explicit-Euler approximation of the velocity time advance, (2) an implicit solution of the free surface elevation (continuity) time advance, and (3) a finite-volume correction of the velocity field to ensure flux conservation, stability, and consistency with continuity [16].

2.3 Stability and flow reversals

As is common in shallow-water models, we model the bottom stresses with a standard drag relationship such that the stress in the x_j direction is

$$\tau_{bj} = \frac{1}{2} C_D \rho u_j \sqrt{u_1^2 + u_2^2} \quad : \quad j \in \{1,2\} \tag{4}$$

where C_D is a drag coefficient. The wind stress in the direction of the wind is modeled as

$$\tau_w = C_{D(w10)} \rho_a \left(\mathbf{U}_{w10} - \mathbf{U}_\eta \cos\beta \right)^2 \tag{5}$$

where $\mathbf{U}_{w10}$ is the wind speed measured at 10 m above the surface, $\mathbf{U}_\eta$ is the water speed at the surface, β is the angle between the wind direction and the water direction, $C_{D(w10)}$ is a drag coefficient based on the 10 m wind measurement height, and ρ_a is the air density. The wind drag in the x_1 and x_2 directions is found from

$$\tau_{w1} = \tau_w \cos\omega \qquad \tau_{w2} = \tau_w \sin\omega \tag{6}$$

where ω is the angle from the x_1 axis to the wind direction.

One of the issues that does not seem to be addressed in the literature is the destabilizing effect that boundary stresses can have in a reversing flow. In the semi-implicit momentum solution of [6] the boundary stresses are defined in terms of the time n values, which implies that the drag between time n and n+1 steps in the implicit solution must oppose the time n flow direction. However, when the flow reverses direction during a time step the explicit drag is effectively an input of momentum, which is destabilizing (i.e., it does not oppose the time n+1 flow direction and is hence anti-dissipative). Although this problem is unlikely to lead to catastrophic instability in simulations of a large-scale estuarine flow where reversals have a long time-scale, it can be a vexing issue in a shallow, wind-driven marsh where reversals are small in spatial-scale and short in time-scale. To fix this

problem, the bottom drag term is time-linearized and solved implicitly as part of the free-surface solution. Specifically, the bottom drag term in Eq. (1) is represented as

$$\frac{\tau_{bj}}{\rho h} = \frac{C_D\, u_j^{n+1}\left(\left[u_1^n\right]^2 + \left[u_2^n\right]^2\right)^{1/2}}{2h^n} \quad : \quad j \in \{1,2\} \tag{7}$$

where n superscripts indicate data at the known time level and $n+1$ superscripts are the unknown solution time level. This approach is similar to time-linearization ideas developed by Patankar [4, 32]. Time-linearization ensures that the bottom drag is always in opposition to the velocity direction at time $n+1$ by moving the drag term from the **b** side of **Ax**=**b** to the **A** side in the matrix inversion step of the semi-implicit method (see [6] for further details of the semi-implicit matrix). This approach guarantees the net effect of drag term is *always* in opposition to the time $n+1$ velocity and thus is always dissipative. Note that simply discretizing drag as an implicit term without this time-linearization is possible, but it creates a nonlinear term of $(u^{n+1})^2$ that destroys the simple linear solution technique at the heart of the semi-implicit method [6]. Failure to use implicit drag discretization can destabilize the solution during flow reversals, which is a particular problem for wind-driven flows in a marsh.

2.4 Wetting and drying

Wetting and drying of tidal flats is always a challenge for numerical modeling and has a wide literature (e.g. [5, 28, 30, 44]). Wetting/drying methods are typically somewhat *ad hoc* and related to the underlying numerical discretization techniques. In the semi-implicit approach, dry cells do not cause instability as they simply imply $\eta^{n+1}=\eta^n=b$ if there are no fluxes into a cell [12]. However, a wetting/drying challenge for the semi-implicit theta-method is that the theory [7] does not constrain the implicit solution of η relative to the bottom elevation b, so it is entirely possible to have a time step where a wet grid cell starting with $\eta^n>b$ will end with $\eta^{n+1}<b$. This unphysical condition is typically remedied with an *ad hoc* clamping of $\eta^{n+1}=b$ to create a dry cell. Unfortunately, as the original solution of $\eta^{n+1}<b$ is volume conservative, such clamping inherently causes non-conservation of volume, which cascades to non-conservation of scalars.

A related problem is that real-world wetting/drying involves thin layers where the flow is strongly affected by the local bottom slope; however, the z-level grid system only represents the dynamic effects of the larger-scale bottom slope between grid cells and does not directly consider the volume effects of the slope within a grid cell itself. Thus, during the model drying process a rapid drawdown can create the conditions shown in Fig. 2 where water on the upstream tidal flats has a dramatically different free surface elevation. If the free surface gradient between the two cells is used as the momentum source for the flow (as in the standard solution algorithm), then extreme unrealistic velocities are produced. The result is typically $\eta^{n+1}<b$ in the next

time step and a large loss of conservation. We solve this problem through an *ad hoc* approach that treats the flow from the upland as though it is similar to flow over weir [46] where the velocity is given by

$$u_f = C_f\sqrt{2gh_f} \tag{8}$$

where u_f is the velocity across the cell face, C_f is an empirical coefficient (herein 0.7) and h_f is the water depth at the face. The u_f computed from time n data can be used directly in the discretization of the free surface evolution (removing the dependency on the free surface pressure gradient across the face), which ensures that the velocity remains limited to physically reasonable values and the drying step to $\eta<b$, if it occurs, will be small.

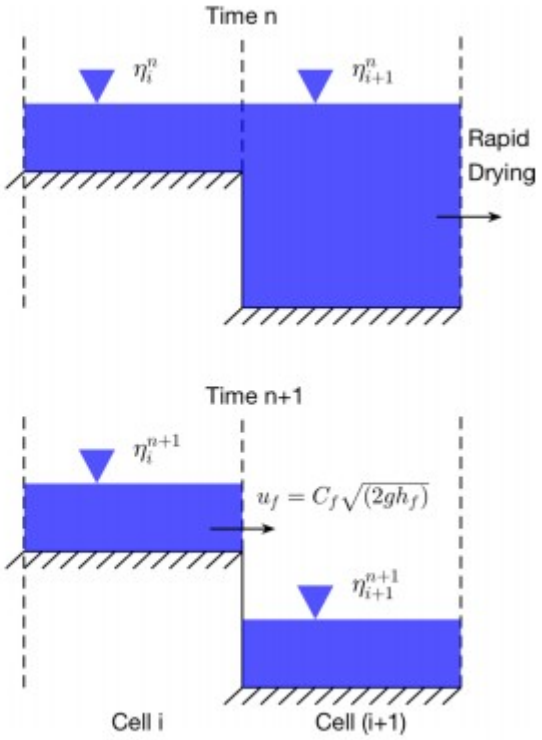

Fig. 2 Rapid drawdown from time n to time $n+1$ leaves water volumes in the uplands with a large driving pressure gradient. At time $n+1$, the steep surface gradient $\eta_i^{n+1} - \eta_{i+1}^{n+1}$ could cause unrealistically high velocity unless Eq. (8) is used to correct the velocity

Rapid wetting can cause a problem similar to rapid drying. For efficient computation of scalar transport, wetting should ideally occur with a wet/dry front that moves less than Δx in a time step (i.e., wetting only dry cells that are adjacent to wet cells), otherwise, the scalar computation must be subtime-stepped to ensure stability. However, the semi-implicit method is stable for $CFL_B>1$, which implies that water can appear in a dry cell that is *not* adjacent to the wet/dry front. These non-adjacent wetting cells typically have very thin layers containing little volume or scalar mass, so the simplest *ad hoc* approach is to maintain these cells as dry until the wet/dry front moves adjacent, which is accomplished with a $CFL_A<1$ limiter for movement of the wet/dry front. This approach necessarily is non-

conservative (similar to other aspects of wet/dry algorithms), but the volumes lost in the tested simulations are negligible.

Finally, to prevent wetting and drying from becoming a computational burden as $h \to 0$, we set a minimum depth such that $h < h_{min}$ results in $\eta = b$ and a small loss of volume. The present work uses $h_{min} = 10^{-3}$h m.

2.5 Thin layers and drag

As water layers get thinner, i.e., $h \to 0$, the bottom drag of Eq. (4) requires an increasing value of C_D to represent the nonlinearly-increasing drag as the flow evolves toward laminar. That is, a Reynolds number defined as $uh\nu^{-1}$ is expected to decrease as the layer thins and result in an increasing C_D [3, 11, 42]. We use a simple buffer layer approach for this problem, similar to [13, 27, 48, 56]. For our implementation, a drag buffer layer thickness (h_{bd}) is defined such that $h < h_{bd}$ provides a linearly-increasing drag from the standard value to a maximum value as $C_{D(b)} = (C_{Dmax} - C_D)(h_{bd} - h)h^{-1}{}_{bd}$. Herein the $C_{Dmax} = 1.0$ and $h_{bd} = 0.1$ m.

The wind acting on thin-layer flows creates further challenges. The empirical wind stress relationship of Eqs. (4) and (5) are based upon data where the wind and bottom boundary layers are effectively separated over a water column of some depth. However, for a sufficiently thin layer, both the wind-stress boundary layer and the bottom boundary layer will take up the entire water column, and simple linear superposition of their effects does not provide an adequate model of nonlinear interactions. That is, in the standard model the energy transfer from the wind is split between turbulent dissipation in the water column and acceleration of the near surface layer, but in a thin layer some portion of the wind effects are directly dissipated at the solid boundary. This issue is critical as simple superposition of standard bottom drag equations and wind-forcing models leads to absurd accelerations of thin-layer flows. To the best of our knowledge, this issue has not been discussed in the literature and there are no empirical data sets looking at the boundary layer interactions at the scales that are typical of tidal marshlands. Ideally, the τ_w model should be independent of the layer thickness and the τ_b model should account for the increased dissipation associated with the interaction of boundary layers. However, maintaining the standard τ_w and increasing τ_b requires a delicate balancing act otherwise the wind-driven velocity tends become unrealistically large. In the absence of data, we found the most practical approach was to provide an exponential decrease in the wind $C_{D(w10)}$ for water depths below a h_{bw}, which can be thought of as a wind buffer layer thickness—similar to but independent of h_{bd} for the drag. Formally we have $C_{D(wb)} = C_{D(w10)} \exp\{-\alpha (h_{bw} - h) h_{bw}^{-1}\}$ where α is a decay coefficient. For the present work we used $h_{bw} = 0.1$ m and $\alpha = 10$.

2.6 Instabilities and the nonlinear advection term

Incipient instabilities in a simulation typically appear as anomalously-large local velocities. In the time-marching algorithm, the nonlinear advection term typically amplifies the anomaly and propagates the instability to adjacent cells. Ideally, a model would never see such an anomaly or would reduce the time step to stabilize any anomaly. It seems generally impossible to ensure that a complex marsh model will be entirely free of instability, and reducing the model time step is simply impractical. Our solution is to sacrifice local fidelity of the discrete equations in order to suppress the growth incipient instabilities—we do this by limiting the nonlinear terms in the momentum solution. We define a nonlinear term limiter with a low cutoff (L_c) and a high cutoff (H_c). For a grid cell where $CFL_A > H_c$, the local nonlinear term is completely suppressed. For a cell where $L_c < CFL_A < H_c$, the discrete nonlinear terms are linearly reduced, i.e. for $N = u\partial u/\partial x$, the reduced nonlinear term is a simple linear decay over the cutoff range: $N_R = N(H_c - CFL_A)/(H_c - L_c)$. In the present work $L_c = 0.5$ and $H_c = 0.7$. The limiter ensures that the high CFL_A at a few points in space/time are not amplified by nonlinearity, which typically then allows the anomaly to be dissipated in the following free-surface solution.

2.7 Advection discretization and channel scales

In general, the literature deprecates the use of 1st-order upwind spatial discretization schemes as too diffusive for practical use. We agree with this philosophy in general, but in the specific application to 2D modeling of a channelized marshes we find higher-order schemes can distort the channel connectivity. Ideally, every channel in a marsh would be discretized by 8 or 10 grid cells across its width, allowing development of horizontal boundary effects and a meaningful ability to use a 3rd-order upwind discretization stencil. As a practical matter, such a discretization would drive the grid mesh down to ~0.1 m, requiring a time step less than 10^{-2} seconds and an impractical (for today's computers) computational time for modeling months (or even days) of marsh hydrodynamics. Once we are forced to a relatively coarse mesh, as is common in many geophysical problems, we encounter practical difficulties in applying a higher-order upwind stencil. *Where a channel is represented with only one or two grid cells across its width and has convoluted S-turns along its length, a higher-order upwind stencil requires extensive exception handling to ensure that the selected scalar values represent the values in the channel and not in the nearby shallows.* Otherwise, the modeled scalar flux in the channel can be driven by out-of-channel values that are entirely unrealistic.

To illustrate this problem, consider Fig. 3 where an 180 m ×180 m area in the Nueces Delta at 30 m ×30 m resolution is presented (see Sect. 2.8 for further details). This area is divided into shallow (brown) and deep (blue) regions to illustrate typical marsh channels on a coarse mesh. It can be seen that the 1st-order upwind stencil (red dots) are guaranteed to include only

in-channel values. In contrast, 3rd-order schemes (white circles) include values in shallow cells that are unlikely to represent either the correct momentum or salinity in the channel. An interpolation stencil in 2D with depth-dependent weighting for the nine upwind cells is a theoretical higher-order solution to this challenge. However, the key difficulty for a 2D stencil is that a channelized area requires extensive exception handling for blocked cell-edges, which will be computationally expensive.

An unfortunate consequence of the use of the 1st-order stencil is that numerical diffusion will be greater than the physical κ of Eq. (3) under most flow conditions. Thus, we expect the model to diffuse any sharp salinity gradients in the marsh, which must be considered in interpreting results.

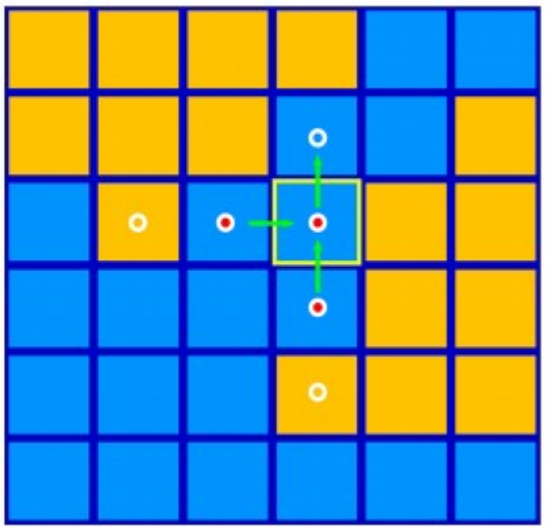

Fig. 3 Stencils for 1st-order upwind (red dots) and 3rd-order upwind (white circles) schemes applied on one 30 × 30 m grid cell (yellow box). The region shown is the Nueces Delta at the intersection between the Rincon Bayou and the Rincon Overflow Channel (ROC) where brown indicates shallow areas whose scalar concentrations may be significantly disconnected from the deeper (blue) channels. The green arrows represent the major fluxes in/out of the target cell

2.8 Bathymetry processing for connectivity

Creating an adequate bathymetry for a marsh requires trade-offs between structural accuracy and practical computability. Modeling directly using the 1×1 m resolution raster bathymetry available for the Nueces Delta is theoretically possible, but would require 7.5×10^7 grid cells and $\Delta t<1$ s, i.e. more than 3.0×10^7 steps per year of simulation. With a numerical model using several hundred floating point operations per grid cell per time step, we would require $O(10^{18})$ floating point operations for a year of simulation. To achieve reasonable simulation times would require a supercomputer in the petaflop range. Although such computers exist, they are not yet readily available to the majority of the scientific community. Furthermore, for larger marsh and delta systems the computational scales required for such high-resolution modeling simply are beyond what we can presently handle.

For the present work, we developed up-scaled raster bathymetries at 15×15 m and 30×30 m grid resolution. The methodology follows the approach in [22] using a median filter to create a coarse-grid raster and a fine-scale (11 m) representation of the resolvable “background” topography, as shown in Fig. 4a, b. It is clear that the filtered bathymetry at the coarse-

grid scale is missing connectivity at <0 m elevation between two depressions in the marsh. The difference between the background topography and the original 1 m fine-resolution topography is used to identify contiguous objects that are not represented in the coarse-grid bathymetry but should have large-scale effects. These can be described as “positive” objects that represent blocking features higher than the coarse-grid bathymetry and “negative” objects that represent unresolved channels. The method for using positive objects to create “cell edge” features at the boundary between two raster cells is described in detail in [22]. A modification of this approach is used herein for negative objects, which are identified as channel grid cells with the bottom elevation adjusted from the median filter value to the median of the negative object. An additional step is taken to find locations where two channel cells are only diagonally connected (i.e. they do not share a common cell face). The bottom is adjusted in a cell perpendicular to the diagonal to create resolved channel bends that maintain connectivity.

The negative object method effectively takes any channel that is narrower than the model grid and broadens it to the grid scale to ensure connectivity. Clearly, this approach maintains connectivity at coarse-grid scales at the cost of physical fidelity in the channel cross-sectional area. To allow a balance between connectivity and fidelity, we ignore identified channels that take less than r fine grid cells in a coarse grid cell, where r is the grid-coarsening ratio (e.g. r=15:1 for the 15×15 m grid developed from 1×1 m data). The result, shown in Fig. 4c, improves the connectivity at the coarse grid scale compared to the median-filtered bathymetry of Fig. 4b, but it is clear that some connectivity at <0 m elevation has not been restored. Developing intelligent and robust automated approaches to ensuring good channel connectivity of fine-scale effects within the coarse model mesh remains an ongoing challenge. In the interim, we have identified key choke points in the marsh that are poorly resolved by the algorithm and restored connectivity by manually adjusting the coarse-grid elevations, as shown in Fig. 4d. The complete 30×30 m bathymetry for the Nueces Delta computational domain is shown in Fig. 5.

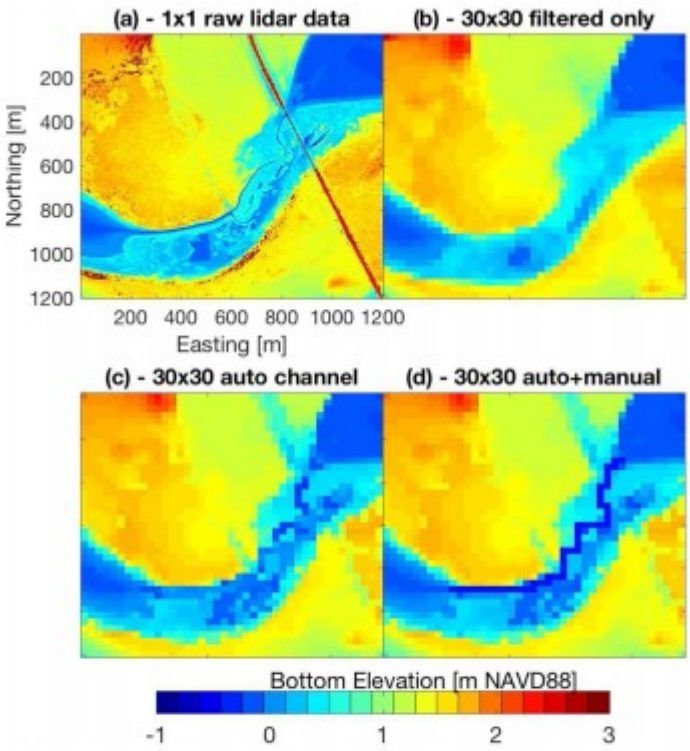

Fig. 4 Bathymetry processing for small section of Nueces Delta: **a** 1 by 1 m lidar data, **b** median filter applied to create coarse grid, **c** after adding automatic channel algorithm and **d** addition of manual channel identification. Note that a narrow channel in the center of (**a**) is totally smoothed on (**b**). The surface connectivity is blocked. Only with the manual channel identification (**d**) we can reconstruct the surface connectivity

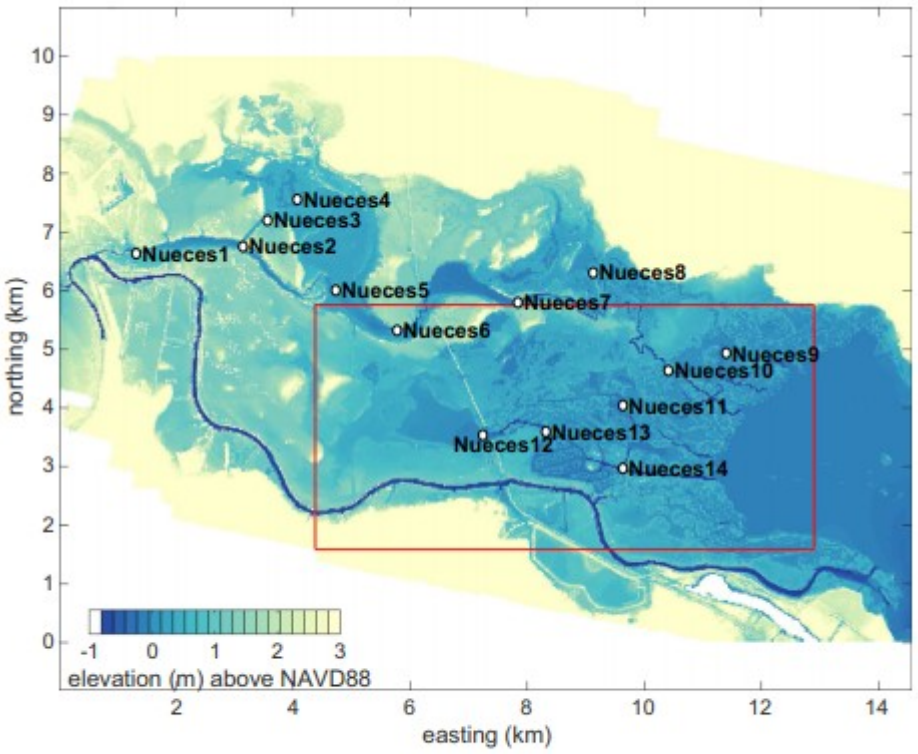

Fig. 5 The 30 by 30 m bathymetry used for NDHM. The locations of 14 field monitoring stations were labeled. More details of these stations can be found in Sect. 3.1. The red box is the computation domain for the stability test

3 Model setup

3.1 Field data

Field data is used for both boundary conditions and calibration. Locations of long term data collection sites used for boundary conditions are shown in Fig. 1. We take the tidal forcing, wind forcing, and upstream pumping to be fundamental processes that are represented with the best available data and are not perturbed in the test cases. Tidal elevations are applied along the open boundary across the width of Nueces Bay on the east side of the domain in Fig. 5. The tidal data was obtained from Station 185 (Nueces Bay) in the Texas Coastal Ocean Observation Network (TCOON[1]), which is located on the south edge of Nueces Bay just outside the computational domain. Salinity data for tidal inflows used TCOON Station 074 (SALT03) which is approximately midway between the north and south shores of Nueces Bay and less than 1 km outside the computational boundary. Wind speed and direction data were obtained from measurements at TCOON Station 069 (Nueces Delta Weather Station). We applied spatially-uniform values for all boundary conditions as there are no available data sources for spatial heterogeneity at the scales of the computational domain. The upstream boundary of the Rincon Bayou was modeled as a fixed water-blocking edge, which represents a swing gate separating the Bayou from the main stem of the Nueces River [47]. Freshwater inflows were added as a volumetric source

term with zero salinity at the pump outlet location (Fig. 1). The pump flow rates were obtained from the Nueces River Authority.[2]

Texas Water Development Board (TWDB), with funding from the US Army Corps of Engineers, conducted a field campaign to measure salinity, water temperature, and water depth at 14 field monitoring stations in the Nueces Delta from August, 2012, through October, 2013. These stations are named Nueces1through Nueces14, with locations shown on Fig. 5. All sampling was with automated logging stations at 15 min intervals. The water velocity was also measured with ADCPs at two locations in the delta, but these data were not used in the present study. Free-surface elevations (relative to NAVD88) were computed from the measured data by TWDB. The free-surface elevation and the salinity are used herein for model-data comparison. Note that field data measured at Nueces13 and Nueces14 have not been used herein as the data were not coherent with data from other stations. These sensors were along the same channel leading to Nueces12, so their data should have been very similar but showed unexplainable discrepancies. We believe that either these sensors malfunctioned or their placement was not correctly recorded in the metadata.

Analysis of field data (not shown) indicates that upstream salinities at all stations except Nueces1 are episodically higher than any salinities observed in Nueces Bay (station 185) over the course of the field study. The implication is that upstream hyper-salinities result from some combination of (i) direct evaporation from surface water, (ii) release of salt that has been concentrated in porewater around plant roots by transpiration, or (iii) release of salt that is concentrated in the drying of episodically-flushed tidal flats. The complexities of these processes creates a modeling challenge. The development of porewater salinities through transpiration has been documented for the Nueces Delta [43], but we do not have enough data to parameterize its scales or release rates across the landscape. Similarly, evaporation and salt storage in tidal flats is known to be an issue in other systems [2, 55], but we do not have adequate data to evaluate whether it is significant in the Nueces Delta. The direct evaporation from surface water is arguably more tractable through the heat budget methods typically applied in coastal or lake/reservoir models (e.g. [52]), but thin water layers in the marsh tends to develop unphysical temperature extrema due to the difficulty in adequately estimating the bottom reflection that limits the effective shortwave absorption. Furthermore, we found that modeling evaporation across the marsh with simple empirical formulas such as Penman’s equation [29, 33] significantly overestimates salinity (results not shown). Given these complexities, evaluating evaporation models is reserved for future work, and the mismatch between model and observed hyper-salinities herein provides an indicator of these unknown and unmodeled processes. During our study period (Feb. 1, 2013 to Jun. 30 2013), precipitation had relatively insignificant effects on salinity (results not shown) and therefore is also neglected.

3.2 Stability test scenarios

To evaluate the performance of the novel stability treatments described from Sects. 2.3 to 2.5, five model scenarios have been executed on a small section of the Nueces Delta bathymetry (shown as the red box in Fig. 5). Field tide and wind data measured at TCOON Station 185 and 069 were applied as boundary conditions. The initial salinity and the tidal salinity were both fixed to 35 psu, so a perfectly conservative model will have no salinity changes inside the domain. However, local violation of $CFL_A>1$ is expected to cause non-conservation of salinity. The reference scenario uses all the novel treatments to prevent possible instability and unrealistic salinity. The other four scenarios are executed by turning off one of the treatments at a time to examine if this treatment helps to maintain stability and conservation. The four treatments to be turned off are (1) the weir equation for rapid drawdown (Sect. 2.4, named *Drying*), (2) the CFL limiter for rapid wetting (Sect. 2.4, named *Wetting*), (3) the implicit treatment of the bottom drag term (Sect. 2.3, named *Drag*) and (4) the wind thin-layer model (Sect. 2.5, named *Wind*). These test scenarios are evaluated by estimating the total amount of salt lost as well as the mean CFL_A over the entire simulations. The salt loss is normalized (divided) by the loss in the reference simulation for ease of comparison. Note that the impacts of the tested treatments also depend on the bathymetry, boundary conditions and simulation configurations. To make sure all four treatments produce non-trivial results, we intentionally chose a large time step (Δt=120s) such that even the reference simulation did not exactly conserve salinity. However, as shown in Sect. 4.1, the salt loss was orders of magnitudes greater in test cases without the stability treatments.

3.3 Full Nueces Delta test scenarios

A key goal of this paper is to quantify how different bathymetry processing methods affect the model skill in predicting surface water elevations and salinity distributions at practical grid resolutions for a coastal marsh. We have developed a suite of six scenarios using different grid resolutions and bathymetry processing techniques, as shown in Table 1. The baseline simulation (A_{30}) uses all the bathymetric treatments at a grid resolution of 30×30 m, which allows for rapid simulations (approximately 20×real time on a desktop computer). The “no treatment” case with a 30×30 m grid (N_{30}) uses only the median filtered bathymetry, e.g. Fig. 4b. The 15×15 m cases (A_{15}, EC_{15}) were the smallest practical resolution for this study as they ran at only 2× real time. Pairwise comparison of scenarios, as listed in Table 2, allows us to distinguish between effects of different processing techniques. Because the designation of manual channels in A_{30} and *A15* is inherently subjective, we decided to interpolate the manual channels from the A_{30} bathymetry to the A_{15} bathymetry to allow the effect of the grid resolution to be analyzed without introducing further manual intervention. The long-term A_{30} simulation was analyzed from Feb. 1, 2013 to Jun. 30, 2013 to examine seasonal variation of the salinity. Other scenarios were

modeled from Jun. 1, 2013 to Jun. 30, 2013, during which several pumping events occurred. The baseline model parameters for A_{30} scenario are listed in Table 3. Issues of model spin-up and drag calibration are discussed in Appendices A and B, respectively.

Table 1 Description of test scenarios for different bathymetry processing methods

Label	Grid size (m)	Cell edge	Auto. channels	Manual channels
A30	30	Yes	Yes	Yes
N30	30	No	No	No
C30	30	No	Yes	No
EC30	30	Yes	Yes	No
A15	15	Yes	Yes	Yes
EC15	15	Yes	Yes	No

Table 2 List of pairwise comparisons

Figure No.	Pairs compared	Interest of study
Figure 8	*A30*:*EC30*	Effect of manual channels
	EC30:*C30*	Effect of edges
	C30:*N30*	Effect of auto channels
Figure 12	*A30*:*A15*	Effect of grid refinement
	A15:*EC15*	Effect of 15 m manual channels

The first column is the corresponding figure numbers showing the results

Table 3 Baseline model parameters

Parameter	Value	Description
Δt (s)	20	Time step
Δx (m)	30	Grid size
Δy (m)	30	Grid size
F (m)	60	Median filter size for grid coarsening
dH (m)	0.2	Minimum object identification height [22]
ν (m^2/s)	0.0001	Eddy viscosity
κ (m^2/s)	0.0001	Eddy diffusivity
h_{bw}, h_{bd} (m)	0.1	Thin layer model depth
C_D	0.01	Bottom drag coefficient
C_{Dmax}	1	Maximum drag coefficient in thin layer
α	10	Decay rate of thin layer wind stress
h_{min} (m)	0.001	Minimum depth allowed
C_f	0.7	Weir coefficient
L_c	0.5	Low cutoff for nonlinear term limiter
H_c	0.7	High cutoff for nonlinear term limiter

4 Results

4.1 Model stability

As the semi-implicit method with θ=1 is strongly dissipative of free-surface oscillations, none of the stability test simulations described in Sect. 3.2 cause the classic infinitely-increasing free surface oscillations that are the signature

of catastrophic instability. However, local instabilities lead to non-conservation in the salinity field that can be readily analyzed. The normalized salt loss for the stability tests can be found in Fig. 6. All four tested treatments are needed for the model to maintain reasonable global salinity conservation. The reference simulation has an average loss of 0.003% of salt mass over the course of 5 simulation days, amounting to an average global change in salinity of less than 3.3×10^{-4} psu. Most notable in Fig. 6 is the dramatic effect of the *Drag* treatment that increases salinity non-conservation by more than six orders of magnitude. Analysis of the CFL_A over the course of the simulations, Table 4, indicates that the effect of switching from the implicit drag term (*Reference*) to the explicit drag term (*Drag*) causes large changes in the velocity field, which cascades to the non-conservation shown in Fig. 6. It can be seen that removing the *Drying*, *Wetting* and *Wind* treatments have smaller hydrodynamic effects, but still cause global salinity non-conservation increase of several orders of magnitude.

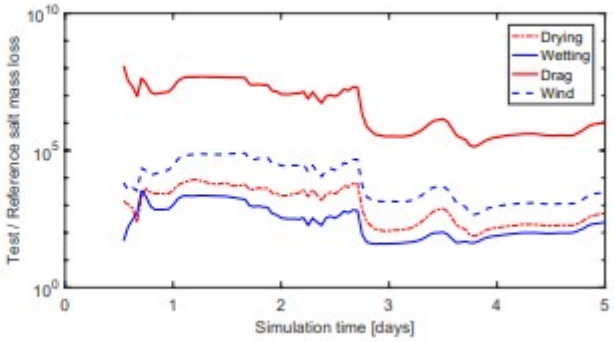

Fig. 6 Ratio of total salt loss between tested scenarios and the reference scenario for 5-day simulations

Table 4 Time-average of spatial max, mean and standard deviation of CFL_A for five stability test scenarios

Scenario	Max.	Mean	SD
Reference	1.5845	0.1392	0.1307
Drying	2.3956	0.1394	0.1319
Wetting	1.5846	0.1392	0.1307
Drag	261.2825	3.3215	18.6116
Wind	1.6790	0.1410	0.1308

4.2 Long-term modeling

The baseline long-term model results are provided by the *A30* case including all the bathymetric treatments. The daily-averaged model-data comparison of free surface elevation and salinity from Feb. 1, 2013 to Jun. 30, 2013 are shown in Fig. 7. For the free surface elevation (left column), the model and field data generally have good agreement. The agreement is excellent in most of the lower delta (Nueces9, Nueces10, Nueces12), which is expected due to proximity to the tidal boundary. At Nueces11 the model systematically overestimates free surface by a small amount. Although we generally hesitate to use model results to question field data, the good

agreement at other stations in the lower delta indicates there is likely a bias in the field sensor vertical datum at Nueces11. The surface elevation agreements in the upper delta stations are not quite as good, but are still reasonable given the complexity of the marsh system. The largest error appears to be an underrepresentation of the water volume retained near Nueces2 between days 140 and 180, which includes pumping events (discussed below). These results likely indicate the model is allowing slightly greater flow rates out of the upper delta than observed in the field, a predictable consequence where the real flow path is narrower than that represented in the coarse-grid bathymetry. Note that blank areas in the field data indicate malfunctioning sensors.

The salinity results (right column in Fig. 7) show that the sudden drop in salinity due to pumping events is clearly captured at most upper delta stations. Hyper-salinity observed prior to pumping at Nueces3, Nueces4, and Nueces6 is not captured in the model, which can be explained by the neglect of evaporation etc. (as discussed in Sect. 3.1). At all other stations, model results are of similar scales as the field data, but with weaker oscillations. This smoothing effect is due to (i) numerical diffusion associated with the 1st order upwind scheme [15], and (ii) the use of the 30×30 m grid, which is not able to capture the subgrid scale features. We do not have a confirmed explanation for the anomalous sustained decline in observed salinity at Nueces10 between day 60 and day 80, which is neither captured in the model nor visible in nearby sensors Nueces8 and Nueces11. Overall, the model shows reasonable agreement in daily averages for both salinity and water surface elevations throughout the marsh for the baseline *A30* case. The increased discrepancies towards the upper delta indicate that bathymetry and surface connectivity have impact on model results as expected, which are investigated in Sects. 4.3 and 4.4.

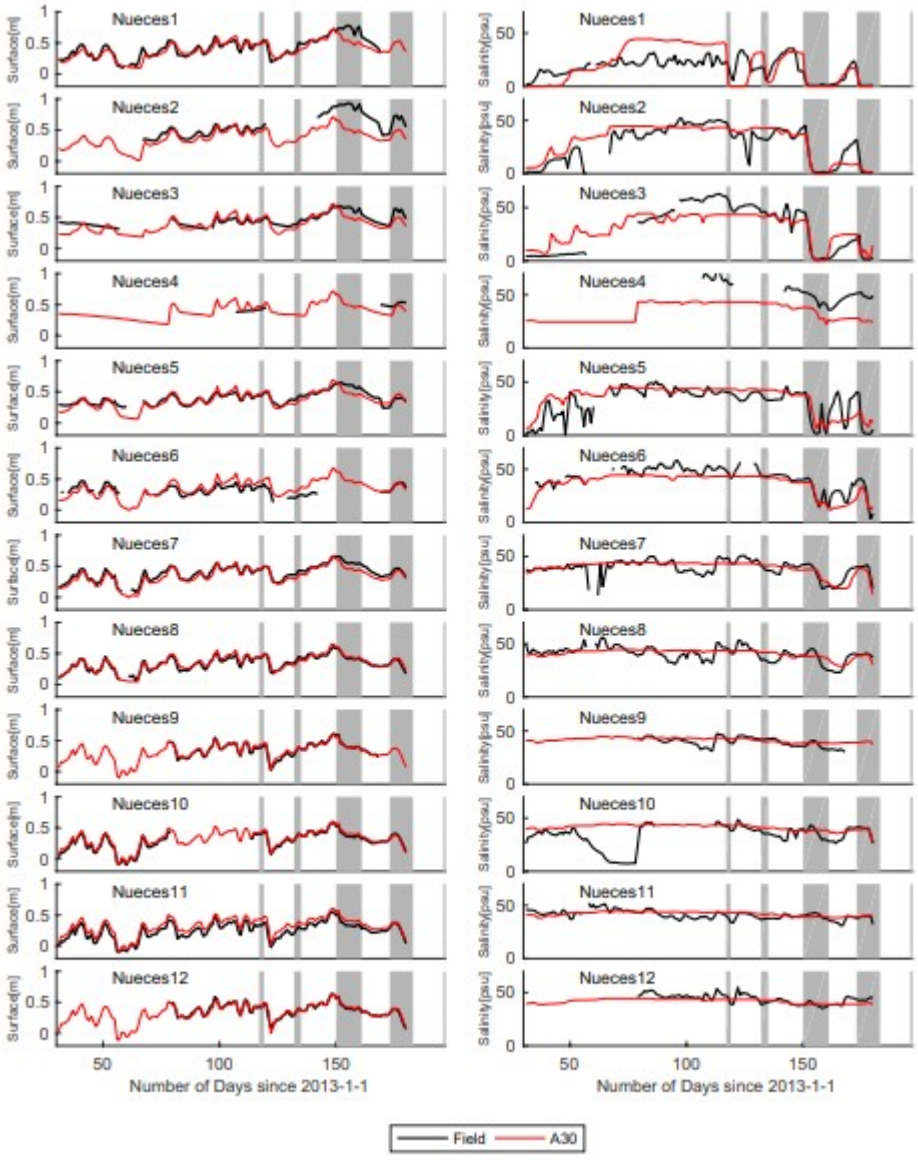

Fig. 7 Daily-averaged modeled and measured surface elevation (left) and salinity (right) at 12 stations from Feb. 1, 2013 to Jun. 30, 2013 (*A30* scenario). Shaded areas represent pumping periods

4.3 Effects of bathymetry treatments

To compare the various bathymetry treatments we focus on a 30-day time frame (Jun. 1, 2013 to Jun. 30) and use hourly rather than daily-averaged data. The results for the *A30*, *EC30*, *C30* and *N30* scenarios are shown in Fig. 8. For the sites in the lower marsh (Nueces7–Nueces12) and the first sensor in the Rincon Bayou upper marsh near the railroad dike (Nueces6), we see that only case *N30* (no treatment) has any substantial difference from the observed surface elevation. These results indicate that the critical requirement for obtaining the correct water surface elevation across the lower delta is the automatic channel identification, which is common to the *C30*, *EC30*, and *A30* cases. The no-treatment *N30* cannot capture the

hourly hydrodynamics in the lower delta, but does provides a somewhat reasonable approximation of longer-term trends. In the upper marsh (Nueces1–Nueces5) the *N30* case is again very poor and is, in many cases, simply flat-lined at the bottom elevation (i.e. no water). That is, the no-treatment condition of *N30* using a simple median filtered 30×30 bathymetry results in bottom elevations that are higher than the observed water at some of the sensor sites. Furthermore, the tidal oscillations are essentially lost in all the *N30* results, indicating that simple filtering to the coarse grid converts the channelized flow in the marshes into sheet flow that rapidly dissipates the tidal energy in the model.

The *C30*, *EC30* and *A30* scenarios produced similar surface elevations at all stations except Nueces1. They all have good model-data agreements at lower delta stations (Nueces8–Nueces12) close to the tidal boundary, but the differences increase moving upstream in the marsh. These results are consistent with the expected accumulation of error associated with shallower flows and more complex topography in the uplands. Nueces1 shows an interesting result where the *C30* and *A30* scenarios capture the tidal oscillations of the water surface shown in the field data, but the *EC30* scenario does not. These results illustrate an important complexity in the interaction between automatic channel identification (*C30*), cell edges (*EC30*), and the manual channel identification (*A30*) in modeling marsh connectivity. Figure 9 shows a high-resolution view of the three model bathymetries in the vicinity of Nueces1. Note that the *C30* bathymetry has connections to the main channel in the east and to the floodplain in the south that are *not* blocked by the channel embankments, which can be identified as cell edges in *EC30*. Thus, it can be expected that simple automatic channel identification without cell edges will overpredict flooding in this area. However, the automated cell edge identification causes blocking of a key flow path at the eastern end of this channel section, which leads to the poor performance of *EC30* upstream of the blockage. The manual channel identification that reduces the bottom elevation in a single cell for *A30* resolves this issue.

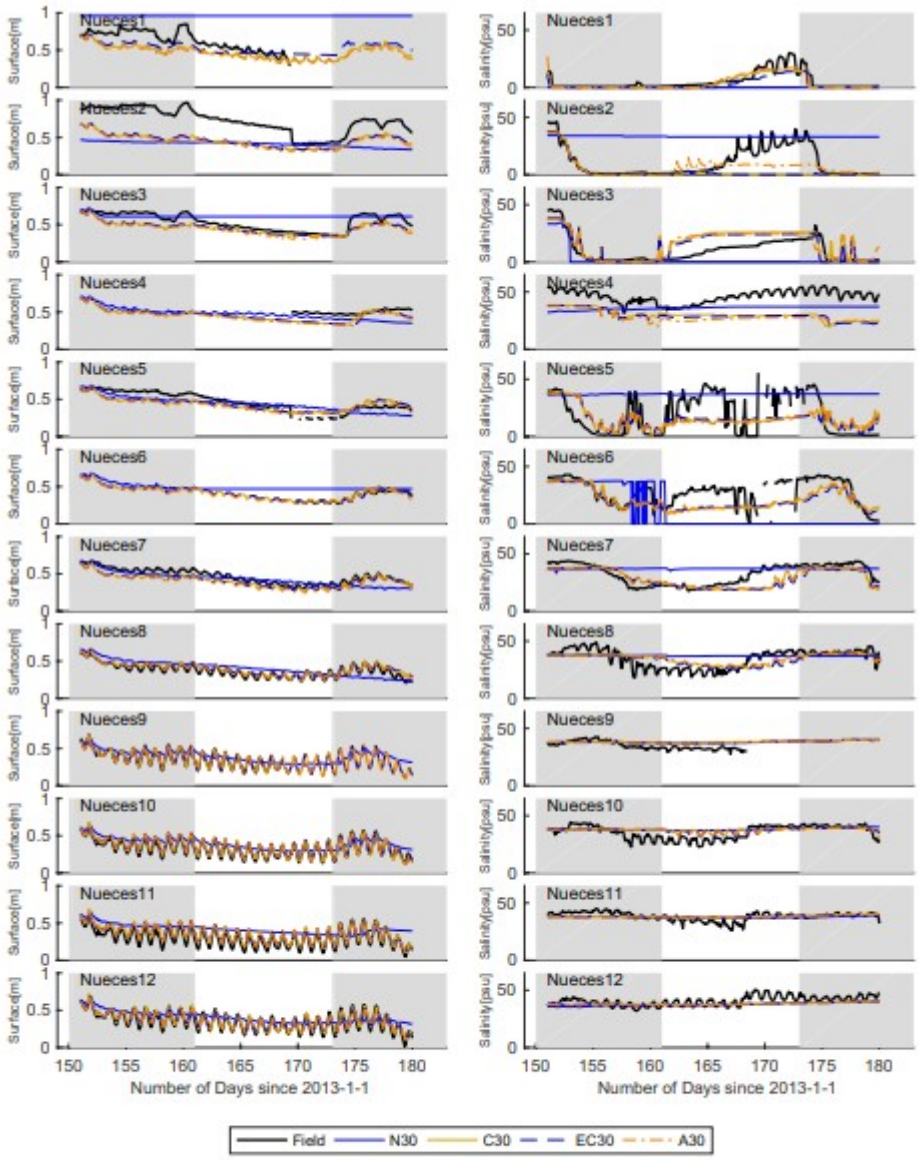

Fig. 8 Hourly modeled and measured surface elevation and salinity at 12 stations from Jun. 1, 2013 to Jun. 30, 2013 for different bathymetry processing methods. The left column is the free surface elevation. The right column is salinity. Shaded areas represent pumping periods

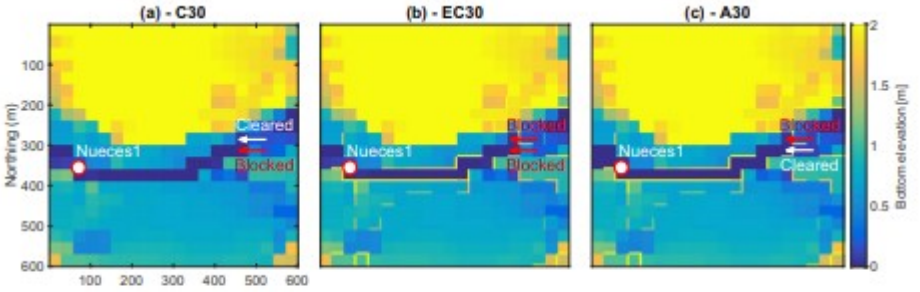

Fig. 9 Bathymetry treatments *C30*, *EC30* and *A30* near Nueces1 that result in surface elevation discrepancies. The surface connectivity between Nueces1 and the lower delta is maintained for *C30* and *A30*, but not for *EC30* (where both flow paths are blocked). The narrow lines between adjacent grid cells represent the cell edges, whose elevations are referred to the colorbar. White arrows indicate cleared flow path; red arrows indicate blocked flow path. The natural downstream flow is from left to right

For salinity in Fig. 8, again the *N30* simulation is inadequate across all cases, indicating that simple coarse-grid filtering of the bathymetry to 30×30 m does not provide an reasonable representation of the connectivity through the marsh. In contrast to the surface elevations results, there is significant divergence in the predictions of the salinity for the different topographic treatments. In the upper marsh (Nueces1), the *A30* with all the topographic treatments shows the strongest salinity signal and matches the overall salinity trend as well as daily oscillations. The other stations in the upper marsh illustrate some of the challenges in modeling evolution of a conserved scalar in convoluted channels. From Nueces1, the flow downstream splits at Nueces2 to travel either through the ROC towards Nueces3 and Nueces4 or down the Rincon Bayou to Nueces5. Flood tides and wind-driven fluxes can reverse these flow directions. When the freshwater pumping operation ends at day 162, the field data shows a slow salinity rise across Nueces2, Nueces3, and Nueces4, with a highly variable pattern at Nueces5. In contrast, the model results (excluding *N30*) show a rapid oscillatory rise of salinity, which becomes relatively constant at Nueces2 and Nueces3. The relatively quick response of the model (compared to field data) at Nueces3 is likely due to (i) the topography-adjusted channels simply allow too much reverse flow rather than slower mixing, and/or (ii) the wind parameterization driving a larger flux in the model. The highly-variable salinity in the field observations at Nueces5 indicates the real world has dynamic mixing features of salt and fresh water that simply are not represented at the resolvable model scales. Modeled salinity in the lower delta, Nueces9, Nueces11, and Nueces12, are smoothed relative to the field observations, indicating the horizontal salinity gradients are being lost in the lower delta such that the model produces a relatively well-mixed system. The similar phenomenon is observed in [26, 54]. However, we see that the main channel through the lower delta (Nueces10) retains some of the oscillatory salinity characteristic.

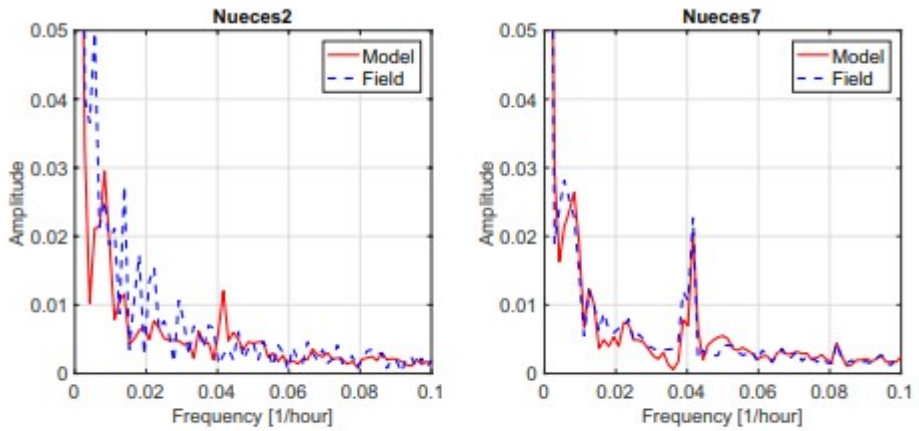

Fig. 10 Amplitude of FFT at upstream (Nueces2) and downstream (Nueces7) stations for field and *A30* model results. The model results capture the tidal frequency (the peaks near frequency of 0.04) at both stations, but the field data only show tidal frequency at Nueces7

Further insight into the model performance is provided by taking a Fast Fourier Transform (FFT) of the free surface displacement at upstream and downstream stations, which should show a power spike at ~0.04 h^{-1} where tidal oscillations are significant. As shown in Fig. 10, both model (*A30*) and field data show a clear tidal signature of similar amplitude at the mid-delta site Nueces7, but at the upper delta site, Nueces2, the tidal signature is entirely missing from the field data, while still detectable (albeit smaller) in the model results. These results indicate that the model does not have sufficient damping of the barotropic mode through the upper delta. This effect likely results from narrower channels being widened to 30 m, which is inherent in the automatic channel algorithm. Note that although tidal oscillation is absent at Nueces2, we can clearly observe the oscillation at Nueces1 from Fig. 8. This result is likely indicative of leaking from the main stem of the river through the upstream swing gate that is normally closed. Note that such leakage would also be a contributor to salinity mismatch in the upper delta.

4.4 Effects of grid refinement

To provide qualitative insight on how grid resolution affects the modeled spatial distribution of salinity, contours at an instant in time are shown in Fig. 11. The selected time (Jun. 12, 2013, 12:00AM) corresponds to the end of an 11-day freshwater pumping event. The sub-figures focus on the West Lake where the *EC30* and *EC15* scenarios show distinct salinity patterns. The high-resolution model (Fig. 11b) creates blockage in the middle of the West Lake, which prevents lateral mixing between the high-salinity water and the pumped water, causing a trapped region of high-salinity water between the middle and upper deltas. The *EC30* scenario (Fig. 11a), on the contrary, shows well-mixed salinity in the West Lake. This is a clear evidence that different grid resolutions lead to difference surface connectivity patterns, which results different spatial distribution of salinity. Figure 11c shows the salinity of the entire model domain (*EC30* with the Nueces Bay masked out).

The middle to lower delta has relatively uniform salinity as observed from Fig. 8.

Quantitative comparisons of field and model results at different grid resolutions using the *A30*, *EC30*, *A15* and *EC15* scenarios are shown in Fig. 12. For the surface elevation, with a few exceptions, the 2× grid refinement does not significantly affect the differences between the modeled and observed. The most notable exception is Nueces1, where the *EC15* and *A15* cases track remarkably better for surface elevation during the pumping periods, but then completely miss the salinity throughout the simulation. For the coarse grid simulations, the frequency analysis (Fig. 10) indicates that tidal oscillations are effectively damped at Nueces2, and therefore the field observations of tidal oscillations further upstream at Nueces1 are a sign of backflow leakage through the NOC (see Fig. 1) from the tidally-influenced main river stem. Thus, the tidal oscillations in the *A30* model (which does *not* allow NOC backflow) indicate that the coarse-grid model has too much downstream connectivity. However, this interpretation creates a conundrum—if the coarse grid allows too much upstream flow, why does it compare better with salinity at Nueces1? The likely answer is in the release of salt bound up in the soils or porewaters of the West Lake tidal flats (Nueces4) that are not represented in the model. Note that the observed salinity at Nueces4 is consistently higher than its neighbors Nueces3 and Nueces5, which is expected for a local salt source. Furthermore, the observations downstream at Nueces5 show strong oscillations indicating frontal mixing that can be interpreted as pumped (fresh) water comes from Rincon Bayou is mixing with high-salinity water from West Lake. With this interpretation, the observed slow rise in salinity in the upper delta after day 160 is primarily attributable to salt released from West Lake being gradually mixed upstream through the ROC rather than water fluxed upstream from the lower delta. Thus the salinity results in the upper delta with the 30×30 m models are the “right” answers for the wrong reasons—i.e. an overestimation of upstream tidal and wind-driven fluxes. In the 15×15 m simulations, since the surface connectivity across the West Lake is blocked (Fig. 11), salinity in the West Lake is not transported further upstream, making the salinities for 15×15 m consistently lower than for the 30×30 m scenarios at Nueces1 through Nueces4. We may conclude that neither grid resolution preserves the 1×1 m surface connectivity—with the 30 m grid overestimates the connectivity downstream of the Rincon Bayou and the 15 m grid underestimates the connectivity across the West Lake.

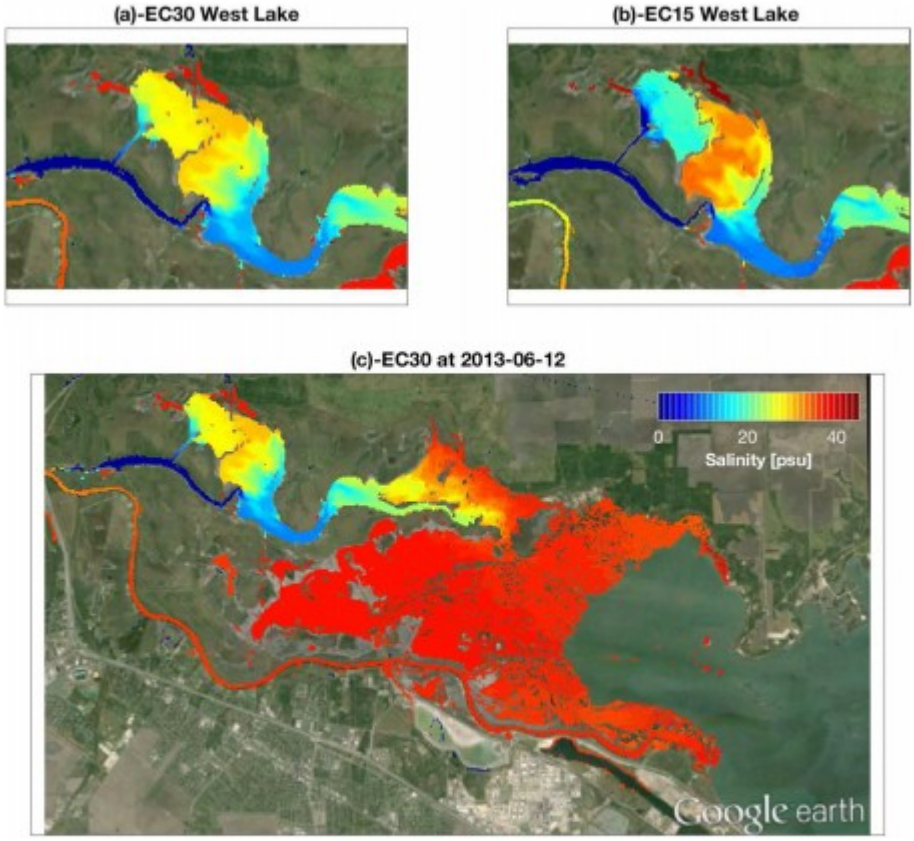

Fig. 11 Modeled salinity in the marsh at 12:00 AM, Jun. 12, 2013. **a** is salinity in the West Lake for the *EC30* scenario, **b** is salinity in the West Lake for the *EC15* scenario, **c** is salinity of the entire model domain for the *EC30* scenario. Note that the open bay hydrodynamics are included in the model, but salinities in the bay are suppressed for clarity. We can observe the longitudinal salinity gradient in the Rincon Bayou, the well-mixed salinities in the lower delta (possibly due to numerical diffusion) and the distinct surface connectivities in the West Lake

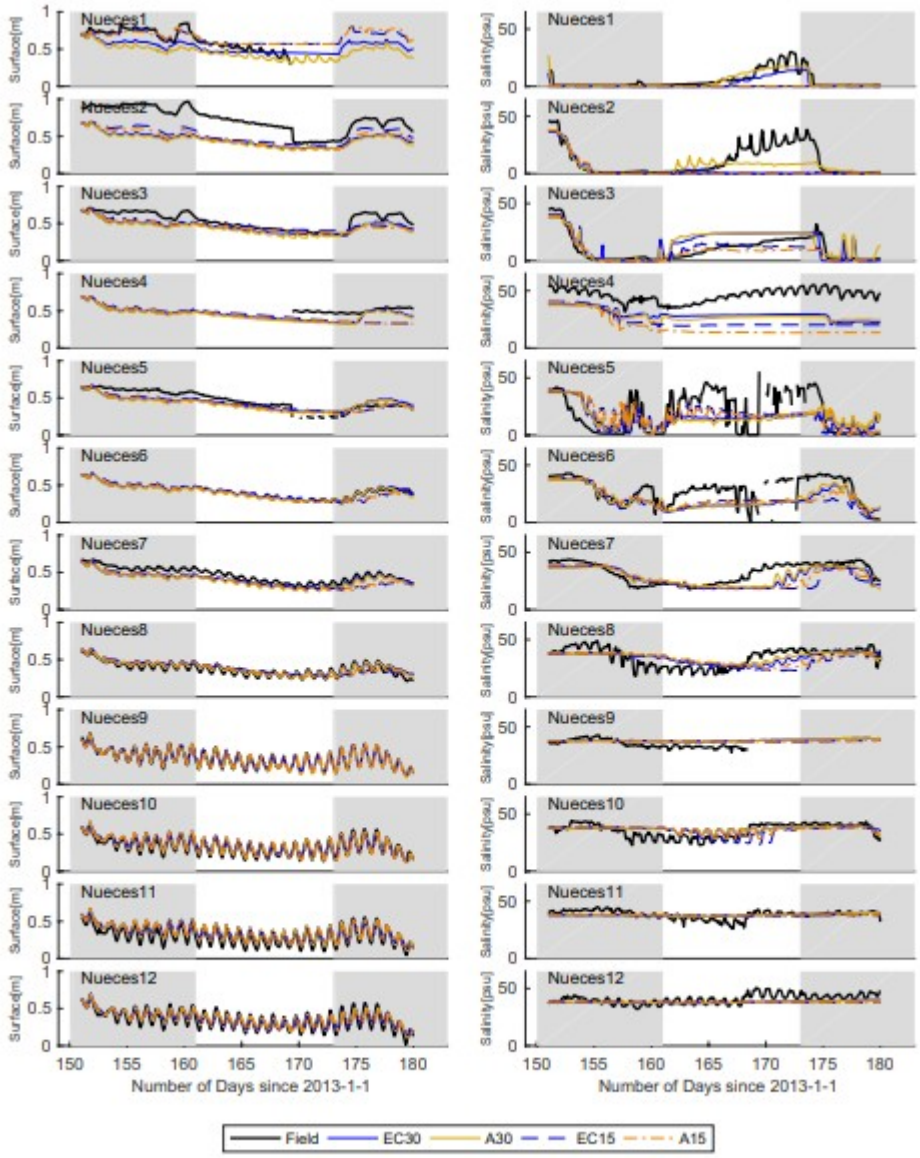

Fig. 12 Grid refinement comparison of hourly modeled and measured surface elevation (left) and salinity (right) from Jun. 1, 2013 to Jun. 30, 2013. Shaded areas represent freshwater pumping periods

5 Discussion and conclusions

The hydrodynamics and salinity transport in a shallow coastal wetland, the Nueces Delta, have been modeled using a 2D depth-integrated numerical model (NDHM) that is designed to handle wetting/drying, thin-layer flows, wind-driven fluxes, and coarse-grid approximations of fine-resolution connectivity. The goal of the present study is to examine if these new algorithms could help to maintain stability and surface connectivity, which are critical challenges that have to be overcame before salinity transport processes in shallow marshes can be modeled and studied. The model results are compared with field data measured at multiple locations in the computation domain on both tidal and sub-tidal time scales. The effects of

grid resolution and various bathymetry processing methods are assessed. The major findings are:

1. The approaches used to handle flow reversal (Sect. 2.3), rapid wetting/drying (Sect. 2.4) and the thin-layer drag models (Sect. 2.5) are effective in maintaining hydrodynamic stability and limiting scalar non-conservation caused by high CFL effects, without requiring subtime stepping.
2. The NDHM is able to produce good model-data agreements for both tidal and sub-tidal free surface elevation in the lower delta, which is closer to the Nueces Bay open boundary. In the upper delta, subgrid topography causes poor surface connectivity and poor results at practical grid resolutions if the bathymetry processing does not explicitly account for subgrid-scale features (channels and blockages).
3. Automatic channel and edge identification from subgrid data provides significant improvement over an untreated coarse-grid bathymetry. Manual channel identification, although time-consuming, further improves the representation of bathymetry on a coarse grid.
4. One drawback in representing fine-scale connectivity at a coarse resolution is that broadening a fine-scale channel to the resolved coarse-grid resolution predictably leads to overestimation of fluxes. It seems likely that either some form of automated spatial adjustment through a drag coefficient or through use of subgrid flow areas is needed to compensate for this effect.
5. The NDHM provides satisfactory model-data agreements for sub-tidal salinity variations, although there is some question as to whether the upstream propagation of high-salinity water is overestimated at 30×30 resolution with the full bathymetry treatment. The downstream propagation of a salinity mixing front during freshwater pumping is qualitatively captured, but quantitative agreement is difficult to obtain due to missing salt sources (e.g. evaporation, porewater salinity).
6. A modest 2× refining of the model grid provides greater insight, albeit at a 10× increase in computational time. The comparison across grid scales shows that the “better” answer for upper delta salinity at the 30×30 m grid scale is likely due to excessive upstream salinity flux taking the place of neglected salinity sources.
7. Simple grid refinement, unless carried out to an extremely fine scale, does not necessarily eliminate bathymetric errors. This effect is illustrated by the 2× grid refinement that interrupts surface connectivity upstream in the West Lake, indicating that an even finer grid is required to represent fluxes through the choke point in this region.

Overall, the model results are promising and show that a coarse-grid model has the potential to capture the fluxes of the salt/fresh water interface in a coastal marsh without requiring micro-resolution and supercomputing resources. Errors in modeled salinity come from multiple aspects such as unresolved bathymetry, inadequate field data, and omitted source terms. It has been shown that shallow-marsh model construction should follow the three requirements proposed in Sect. 1, where maintaining stability and surface connectivity are critical challenges and prerequisites for salinity modeling. With the stability issue being properly handled in this study, the key future tasks for improving such models are (i) developing improved automated approaches that correctly represent flow connectivity/blockages along with the resistance of fine-scale features project up to the coarse-grid scale, and (ii) developing algorithms and approaches for modeling salinity storage and exchange between surface water, porewater, soil, and plants.

Footnotes

1. https://cbiweb.tamucc.edu/TCOON/.

2. http://www.nueces-ra.org/CP/CITY/rincon/.

3. https://www.mathworks.com/matlabcentral/fileexchange/29025-ordinary-kriging.

Acknowledgements

This work has been supported by the Texas Water Development Board under interagency cooperation contracts 1400011719 and 1600011928. Field work was conducted by the TWDB with funding from the US Army Corps of Engineers.

Appendix A. Model spin up

The “spin-up” time for a model is the simulation time that it takes for the results to be independent of the initial conditions. Spin-up for a fresh/salt marsh simulation is inherently challenging. Unless the sampling period includes a complete flush of the system, we cannot start from a “clean slate” of zero salinity and expect to reach the actual salinity distribution by some date. In contrast, the hydraulic memory of the velocity and elevation fields is relatively short and can be approximated by the time it takes for an increase in tidal elevation to be seen throughout the domain, which allows uniform conditions to be readily applied as a starting guess. To examine the spin-up behavior of the NDHM, we conducted test simulations starting two weeks apart (from Nov. 15 and Dec. 1, 2012 respectively) to evaluate when the model results are independent of the initial starting date. The start date was chosen based on availability of field data and to ensure sufficient spin-up time prior to the pump operations in summer. Note that during the winter, the secular water elevations in the Nueces and Corpus Christi Bay systems are declining towards a semi-annual low in January [50], and it can be expected that spin-up times during other stages of the secular cycle might

be different. For the spin-up simulations, the NDHM was started from quiescent water (u_j=0,j∈{1,2}) with a uniform free-surface elevation equal to the tidal boundary condition. The initial condition for salinity was computed using the ordinary kriging method,[3] in which the salinity field was interpolated based on measurements from the 12 stations at the beginning of the model start date.

We consider an adequate spin-up time as the interval when the residual (difference between 2 simulation results) is less than 2 psu for salinity and 0.002 m for free surface. Using this metric, the spin-up times as well as a final salinity residual after 60 days from Dec. 1, 2012 are listed in Table 5. As expected, the spin-up times for free surface elevation are significantly shorter than that for salinity. The poorest result was at Nueces4 in the upstream tidal flat known as West Lake (Fig. 1) that is poorly flushed during the secular low tidal period in winter. In contrast, the locations in the Rincon Bayou main channel and marsh areas close to the open boundary (e.g. Nueces1, 5, 6, 7, 9, 10 and 11) see more consistent flushing through the winter and hence the spin-up times are much shorter. As a conservative measure, all data analyses herein is based on model results after 60 days of spin-up time.

Table 5 Spin-up time for free surface elevation, salinity and 60-day residual for salinity at each TWDB station

Station No.	Spin-up (days)		Res. (psu)	Station No.	Spin-up (days)		Res. (psu)
	Free surf.	Salinity	Salinity		Free surf.	Salinity	Salinity
Nueces1	6	8	0	Nueces7	6	40	0.40
Nueces2	6	17	0.42	Nueces8	6	50	1.18
Nueces3	10	58	1.43	Nueces9	< 1	28	0.52
Nueces4	10	> 60	6.58	Nueces10	1	40	0.55
Nueces5	6	20	0.44	Nueces11	< 1	35	0.29
Nueces6	6	20	0.44	Nueces12	1	50	1.36

The 60-day residuals for free surface elevation are all on the order of 10^{-4} m or less

Appendix B. The irrelevance of global drag calibration

Model calibration for a 2D shallow-water model is generally accomplished by adjusting either coefficients of a turbulence model (e.g. ν) or drag (C_D) that control energy dissipation [34, 53]. This is typically conducted using global values: the calibration problem cannot be reasonably constrained if every model grid cell has an independent C_D and field data is available at limited locations. Our analyses (not shown) indicate the NDHM results are relatively insensitive to the choice of a global ν or C_D. The minor variability of results obtained in our calibration exercise does not allow rejection of the hypothesis that our *a priori* selected baseline values are acceptable. Similar conclusions have been reached by other researchers for simulations with complex bathymetries [9, 35].

Arguably, there are two principal reasons for the insensitivity of the model to calibration: (i) the numerical dissipation associated with our 1st-order upwind advection scheme [14, 15], and (ii) the "topographic" dissipation associated with the convoluted channels in a marsh. We have not seen this latter topic specifically addressed in the literature, but it follows from simple consideration of how momentum turns a corner with the hydrostatic approximation. In the real world, the pressure gradients at a channel bend serve to redirect momentum, i.e. the dp/dx_1 required to slow momentum in the x_1 direction increases the pressure p on the outer edge of the channel, and results in dp/dx_2 that accelerates the flow in the x_2 direction around the bend. Thus, streamwise momentum is not lost around a corner, but is smoothly transferred from x_1 to x_2 coordinate directions through the pressure gradients and nonlinear terms. Indeed, the 1D Saint-Venant equations for channel flow are essentially the mathematical embodiment of this idea [21]. However, when a narrow channel bend is represented by a single set of grid cells in a 2D hydrostatic model, only a small part of the momentum change in the x_1 direction will be recovered in the hydrostatic pressure and returned to the x_2 direction. The fundamental problem is that insufficient grid resolution at the channel scale creates an inability to have smooth transition of pressure gradients and nonlinear terms between coordinate directions. Thus, every bend in a narrow channel causes the flow to stop its streamwise acceleration in the x_1 direction and restart the streamwise acceleration in the x_2 direction. If the marsh system were strongly nonlinear with high channel velocities, then increased grid resolution would be necessary for a reasonable approximation of the fluxes. However, velocities in the marsh channels are slow and only weakly nonlinear, so relatively coarse grid resolution of the channels is an acceptable trade-off for computational efficiency. The main consequence is that the topographic dissipation from channel bends plays a major role in dissipation of energy, which makes C_D, ν, and drag calibration nearly irrelevant.

It can be argued that a depth-dependent drag model (e.g. Chezy–Manning $C_D = g\hat{n}^2 h^{-1/3}$, where $\hat{n}$ is Manning's n) would be an appropriate baseline model. However, our calibration exercises showed that field data could not adequately discriminate between competing models. Thus, we appeal to Occam's Razor and use the simplest possible drag model. This model is a baseline uniform C_D that is only depth-dependent in thin layers (as discussed in Sect. 2.5) where the depth dependency has a clear impact. Nevertheless, we do not consider this the final answer. Results with the automated channel bathymetry treatment (discussed below) indicate that some form of spatially-distributed drag might be useful, although it is not clear that simple depth-dependency such as Chezy–Manning is necessarily the solution. We speculate that a local drag coefficient might be linked to the approximations made in the channel connectivity algorithm and calibrated with some form of global coefficient. This idea remains an area of ongoing research.

References

1. Alexander H, Dunton K (2002) Freshwater inundation efects on emergent vegetation of a hypersaline salt marsh. Estuaries 25(6B):1426–1435 2. Alvarez M, Carol E, Dapena C (2015) The role of evapotranspiration in the groudwater hydrochemistry of an arid coastal wetland (Peninsula Valdes, Argentina). Sci Total Environ 506–507:299–307. https://doi.org/10.1016/j.scitotenv.2014.11.028 3. Bricker J, Inagaki S, Monismith G (2005) Bed drag coefcient variability under wind waves in a tidal estuary. J Hydraul Eng 131(6):497–508. https://doi.org/10.1061/(ASCE)0733-9429(2005)131:6(497) 4. Burchard H, Deleersnijder E, Meister A (2003) A high-order conservative Patankar-type discretisation for stif systems of production–destruction equations. Appl Numer Math 47:1–30. https://doi. org/10.1016/S0168-9274(03)00101-6 5. Candy AS (2017) An implicit wetting and drying approach for non-hydrostatic baroclinic fows in high aspect ratio domains. Adv Water Resour 102:188–205. https://doi.org/10.1016/j.advwa tres.2017.02.004 6. Casulli V (1990) Semi-implicit fnite-diference methods for the 2-dimensional shallow-water equations. J Comput Phys 86:56–74 7. Casulli V, Cattani E (1994) Stability, accuracy and efciency of a semi-implicit method for threedimensional shallow water fow. Comput Math Appl 27(4):99–112 8. Casulli V (1999) A semi-implicit fnite diference method for non-hydrostatic free-surface fows. Int J Numer Methods Fluids 30:425–440 9. Cea L, French JR, Vazquez-Cendon ME (2006) Numerical modeling of tidal fows in complex estuaries including turbulence: an unstructured fnite volume solver and experimental validation. Int J Numer Methods Eng 67:1909–1932. https://doi.org/10.1002/nme.1702 10. Cea L, French JR (2012) Bathymetric error estimation for the calibration and validation of estuarine hydrodynamic models. Estuar Coast Shelf Sci 100:124–132. https://doi.org/10.1016/j.ecss.2012.01.004 11. Chao X, Jia Y, Douglas Shields F Jr, Wang SSY, Cooper CM (2008) Three-dimensional numerical modeling of cohesive sediment transport and wind wave impact in a shallow oxbow lake. Adv Water Resour 31:1004–1014. https://doi.org/10.1016/j.advwatres.2008.04.005 12. Cheng RT, Casulli V, Gartner JW (1993) Tidal, residual, intertidal mudfat (TRIM) model and its applications to San Francisco Bay. Calif Estuar Coast Shelf Sci 36:235–280 13. Chou Y, Holleman R, Fringer OB, Stacey MT, Monismith SG, Kosef JR (2015) Three-dimensional wave-coupled hydrodynamics modeling in South San Francisco Bay. Comput Geosci 85:10–21. https ://doi.org/10.1016/j.cageo.2015.08.010 14. Chua V, Fringer OB (2011) Sensitivity analysis of three-dimensional salinity simulations in North San Francisco Bay using the unstructured-grid SUNTANS model. Ocean Model 39:332–350. https://doi. org/10.1016/j.ocemod.2011.05.007 15. Gross ES, Kosef JR, Monismith SG (1999) Evaluation of advective schemes for estuarine salinity simulations. J Hydraul Eng 125(1):32–46 16. Gross ES, Bonaventur L, Rosatti G (2002) Consistency with continuity in conservative advection schemes for free-surface models. Int J Numer Methods Fluids 38:307–327 17.

Hajduk H, Hodges BR, Aizinger V, Reuter V (2018) Locally fltered transport for computational efciency in multi-component advection-reaction models. Environ Model Softw 102:185–198 18. Herbert ER, Boon P, Burgin AJ, Neubauer SC, Franklin RB, Ardon M, Hopfensperger KN, Lamers LPM, Gell P (2015) A global perspective on wetland salinization: ecological consequences of a growing threat to freshwater wetlands. Ecosphere 6(10):206. https://doi.org/10.1890/ES14-00534.1 19. Hill EM, Tunnell JW, Nicolau BA (2015) Spatial and temporal efects of the Rincon Bayou Pipiline on hypersaline conditions in the Lower Nueces Delta, Texas, USA. Tex Water J 6(1):11–32 20. Hodges BR (2014) A new approach to the local time stepping problem for scalar transport. Ocean Model 77:1–19. https://doi.org/10.1016/j.ocemod.2014.02.007 21. Hodges BR, Liu F (2014) Rivers and electric networks: crossing disciplines in modeling and simulation. Found Trends Electron Des Autom 8(1):1–116. https://doi.org/10.1561/1000000033 22. Hodges BR (2015) Representing hydrodynamically important blocking features in coastal or riverine lidar topography. Nat Hazards Earth Syst Sci 56:1011–1023. https://doi.org/10.5194/nhess d-3-1427-2015 23. Hodges BR, Imberger J, Saggio A, Winters K (2000) Modeling basin-scale internal waves in a stratifed lake. Limnol Oceanogr 47(7):1603–1620 24. Hodges BR (2004) Accuracy order of Crank–Nicolson discretization for hydrostatic free surface fow. ASCE J Eng Mech 130(8):904–910. https://doi.org/10.1061/ (ASCE)0733-9399(2004)130:8(904) 25. Hodges BR, Rueda FJ (2008) Semi-implicit two-level predictor-corrector methods for non-linearly coupled, hydrostatic, barotropic/baroclinic fows. Int J Comput Fluid Dyn 22(9):593–607. https://doi.org/10.1080/10618560802353389 26. Inoue M, Park D, Justic D, Wiseman WJ Jr (2008) A high-resolution integrated hydrology-hydrodynamic model of the Barataria Basin system. Environ Model Softw 23:1122–1132. https://doi.org/10.1016/j.envsoft.2008.02.011 27. Ip JTC, Lynch DR, Friedrichs CT (1998) Simulation of estuarine fooding and dewatering with application to Great Bay. New Hamps Estuar Coast Shelf Sci 47:119–141 28. Martins R, Leandro J, Djordjevic S (2018) Wetting and drying numerical treatments for the Roe Riemann scheme. J Hydraul Res 56(2):256–267. https://doi.org/10.1080/00221686.2017.1289256 29. McMahon TA, Peel MC, Lowe L, Srikanthan R, McVicar TR (2013) Estimating actual, potential, reference crop and pan evaporation using standard meteorological data: a pragmatic synthesis. Hydrol Earth Syst Sci 17:1331–1363. https://doi.org/10.5194/hess-17-1331-2013 30. Medeiros SC, Hagen SC (2013) Review of wetting and drying algorithms for numerical tidal fow models. Int J Numer Methods Fluids 71:473–487. https://doi.org/10.1002/fd.3668 31. Murillo J, Garcia-Navarro P, Burguete J (2009) Conservative numerical simulation of multi-component transport in two-dimensional unsteady shallow water fow. J Comput Phys 228:5539–5573. https://doi.org/10.1016/j.jcp.2009.04.039 32. Patankar SV (1980) Numerical heat transfer and fuid fow. McGraw-Hill, New York 33. Penman HL (1948) Natural evaporation from open water, bare soil and grass. Proc R Soc Lond A

193:120–145 34. Ralston DK, Geyer WR, Lerczak JA (2010) Structure, variability, and salt fux in a strongly forced salt wedge estuary. J Geophys Res 115:C06005. https://doi.org/10.1029/2009JC005806 35. Rayson MD, Gross ES, Fringer OB (2015) Modeling the tidal and sub-tidal hydrodynamics in a shallow, micro-tidal estuary. Ocean Model 89:29–44. https://doi.org/10.1016/j.ocemod.2015.02.002 36. Del Rosario EA, Montagna PA (2018) Efects of the Rincon Bayou pipeline on salinity in the upper nueces delta. Tex Water J 9(1):30–49 37. Rueda FJ, Sanmiguel-Rojas E, Hodges BR (2007) Baroclinic stability for a family of two-level, semi-implicit numerical methods for the 3D shallow water equations. Int J Numer Methods Fluids 54(3):237–268. https://doi.org/10.1002/fd.1391 38. Ryan AJ, Hodges BR (2011) Modeling hydrodynamic fuxes in the nueces river delta, center for research in water resources, University of Texas at Austin, CRWR Online Report 11-07, p 92 39. Schoenbaechler C, Negusse S, Guthrie CG (2014) Nueces Delta data collection for calibration and validation of the Nueces Delta Hydrodynamic Model, Technical Report, Bay and Estuaries Program, Surface Water Resources Division, Texas Water Development Board 40. Silva CP, Marti CL, Imberger J (2014) Horizontal transport, mixing and retention in a large, shallow estuary: Rio de la plata. Environ Fluid Mech 14:1173–1197. https://doi.org/10.1007/s1065 2-013-9330-3 41. Snedden GA, Cretini K, Patton B (2015) Inundation and salinity impacts to above- and belowground productivity in Spartina patens and Spartina alternifora in the Mississippi River deltaic plain: Implications for using river diversions as restoration tools. Ecol Eng 81:133–139. https://doi. org/10.1016/j.ecoleng.2015.04.035 42. Spitz Y, Klinck J (1998) Estimate of bottom and surface stress during a spring-neap tide cycle by dynamical assimilation of tide gauge observations in the Chesapeake Bay. J Geophys Res 103(C6):12761–12782 43. Stachelek J, Dunton KH (2013) Freshwater infow requirements for the Nueces Delta, Texas: Spartina alternifora as an indicator of ecosystem condition. Tex Water J 4(2):62–73 44. Teng J, Jakeman AJ, Vaze J, Croke BFW, Dutta D, Kim S (2017) Flood inundation modelling: a review of methods, recent advances and uncertainty analysis. Environ Model Softw 90:201–216. https://doi.org/10.1016/j.envsoft.2017.01.006 45. Torres R, Styles R (2007) Efects of topographic structure on salt marsh currents. J Geophys Res 112:F02023. https://doi.org/10.1029/2006JF000508 46. Tracy H (1957) Discharge characteristics of broad-crested weir. Technical report, Geological Surface Circular, 397 47. Tunnell JW, Lloyd L (2011) Efects of Rincon Bayou Pipeline infows on salinity structure within the Nueces Delta, Texas, Corpus Christi (Texas): Coastal Bend Bays & Estuaries Program project 1106, CBBEP-76. p 23 48. Wang B, Fringer OB, Giddings SN, Fong DA (2009) High-resolution simulations of a macrotidal estuary using SUNTANS. Ocean Model 28:167–192. https://doi.org/10.1016/j.ocemod.2008.08.008 49. Wadzuk BM, Hodges BR (2009) Hydrostatic versus nonhydrostatic Euler-equation modeling of nonlinear internal waves. ASCE J Eng Mech 135(4):1069–1080. https://doi.org/10.1061/ (ASCE)0733-9399(2009)135:10(1069) 50. Ward GH (1997) Process and trends of circulation within the corpus christi bay national

estuary program study area, Publication CCBNEP-21. Coastal Bend Bays & Estuaries Program, Corpus Christi, Texas, p 381. http://cbbep.org/publications/CCBNEP21.pdf 51. Watson EB, Szura K, Wigand C, Raposa KB, Blount K, Cencer M (2016) Sea level rise, drought and the decline of Spartina patens in New England marshes. Biol Conserv 196:173–181. https://doi. org/10.1016/j.biocon.2016.02.011 52. Wunderlich WO (1972) Heat and Mass Transfer Between a Water Surface and the Atmosphere, Water Resources Research Laboratory Report No. 14, Tennessee Valley Authority Report No. 0-6803, Norris Tennessee 53. Yuan D, Lin B, Falconer RA (2007) A modelling study of residence time in a macro-tidal estuary. Estuar Coast Shelf Sci 71:401–411. https://doi.org/10.1016/j.ecss.2006.08.023 54. Zacharias I, Gianni A (2008) Hydrodynamic and dispersion modeling as a tool for restoration of coastal ecosystems. Application to a re-fooded lagoon. Environ Model Softw 23:751–767. https://doi. org/10.1016/j.envsoft.2007.09.007 55. Zhang C, Li L, Lockington D (2014) Numerical study of evaporation-induced salt accumulation and precipitation in bare saline soils: mechanism and feedback. Water Resour Res 50:8084–8106. https://doi.org/10.1002/2013WR015127 56. Zheng L, Chen C, Liu H (2003) A modeling study of the Satilla River Estuary, Georgia: fooding-drying process and water exchange over the salt marsh-estuary-shelf complex. Estuaries 26(3):651–669